Int. J. Heat Mass Transfer. Vol. 31, No. 4, pp. 863–873, 1988
Printed in Great Britain

0017–9310/88 $3.00 + 0.00

Natural convection induced drag forces on spheres at low Grashof numbers: comparison of theory with experiment

D. R. DUDEK
Massachusetts Institute of Technology, Chemical Engineering Department, Cambridge, MA 02139, U.S.A.

T. H. FLETCHER
Combustion Research Facility, Sandia National Laboratory, Livermore, CA 94550, U.S.A.

J. P. LONGWELL
Massachusetts Institute of Technology, Chemical Engineering Department, Cambridge, MA 02139, U.S.A.

and

A. F. SAROFIM
Massachusetts Institute of Technology, Chemical Engineering Department, Cambridge, MA 02139, U.S.A.

(*Received* 12 *March* 1987 *and in final form* 31 *August* 1987)

Abstract—When a heated solid sphere is introduced into an ambient fluid, a natural convective flow occurs which results in a drag force on the sphere. For 10–250 μm diameter particles, the drag force may be as great as the particle weight. This study involves the experimental measurement and the numerical calculation of both the steady-state and the transient natural convective drag force around spheres at low Grashof numbers. The experimental measurements were performed in an electrodynamic balance for Grashof numbers ranging from 0.002 to 0.03. Numerical solutions, based on techniques used by Geoola and Cornish (*Int. J. Heat Mass Transfer* **24**, 1369–1379 (1981); **25**, 1677–1687 (1982)), are computed for Grashof numbers ranging from 0.0004 to 0.5. Comparison of the experimental results to the numerical results show good agreement.

INTRODUCTION

THE ELECTRODYNAMIC balance is a device capable of suspending a single, charged 1–250 μm particle in an ambient gaseous environment and is now being developed as a tool for studying single particle high temperature gas–solid reactions. A vertical force balance on an unheated suspended particle reveals that

$$mg = qE \tag{1}$$

where m is the particle mass, g the gravitational acceleration, q the number of excess charges on the suspended particle, and E the electric field strength in the vertical direction. If no other forces are acting on the particle, changes in particle mass can be followed continuously by monitoring the electric field strength required for particle balancing. Upon laser heating of the suspended particle, however, the fluid near the particle surface is heated due to conduction. Since the ambient fluid is cool, the fluid near the particle surface rises, and a natural convective flow field is set up which introduces a natural convective drag force, F_{nat}, on the particle. The vertical force balance now becomes

$$mg = qE + F_{nat}. \tag{2}$$

This upward drag force on the particle complicates interpretation of the particle weight change data. Arnold and Lewittes [3] were the first to report such a force. Later, Spjut [4] reported drag force magnitudes as great as the particle mass. In order to determine particle reaction rate, changes in particle mass must be distinguished from changes in drag force. Therefore, characterization of the natural convective drag force is necessary if the electrodynamic balance is to be used for continuous mass vs time measurements. Due to the small size of the particles being examined in the electrodynamic balance, the corresponding Grashof number will also be small, with the range of interest being between 0.0005 and 1.0. The Reynolds number is much less than one.

Experimental studies of natural convection around a heated sphere at small Grashof number have been conducted by Meyer [5], Elenbaas [6], Ranz and Marshall [7], Mathers *et al.* [8], Tsubouchi and Sato [9], and Yuge [10]. These authors, however, were interested in heat transfer, and only measured the overall Nusselt number. No experimental measurements of

NOMENCLATURE

C	dimensionless chamber constant, 0.4
C_{DP}	dimensionless pressure drag force coefficient
C_{DF}	dimensionless viscous drag force coefficient
C_{DT}	dimensionless total drag force coefficient
C_p	heat capacity of surrounding gas at constant pressure per unit mass [$m^2 s^{-2} K^{-1}$]
E	electric field strength in vertical direction [$V m^{-1}$]
F_{nat}	natural convective drag force [N]
F_{Stokes}	Stokes' drag force [N]
g	gravitational acceleration, 9.81 $m s^{-2}$
G	modified dimensionless vorticity
Gr	Grashof number, $g\beta(T_s - T_\infty)R^3/\nu^2$
k	surrounding gas thermal conductivity [$kg m s^{-3} K^{-1}$]
K_0	dimensionless pressure at the front stagnation point
K_θ	dimensionless pressure at the sphere surface
m	mesh size in the z-direction
M	number of mesh points in the z-direction
n	mesh size in the θ-direction
N	number of mesh points in the θ-direction
Nu	overall Nusselt number
Nu_θ	local Nusselt number
Pr	Prandtl number, $C_p\mu/k$
q	total excess charge on particle [C]
r	dimensionless radial direction
$\tilde{r}$	dimensional radial distance [m]
R	particle radius [m]
t	dimensionless time
$\tilde{t}$	dimensional time [s]
T	dimensionless temperature
$\tilde{T}$	dimensional temperature [K]
T_s	particle surface temperature [K]
T_∞	ambient gas temperature [K]
u	dimensionless velocity
$\tilde{u}$	dimensional velocity [$m s^{-1}$]
v	velocity of surrounding gas [$m s^{-1}$]
$V_{d.c.}$	balancing d.c. voltage across endcap electrodes [V]
V_i	balancing voltage of unheated particle [V]
ΔV	change in balancing voltage between unheated and heated particle [V]
W	general continuous function representing T, G, and ψ
z	modified dimensionless radial direction
z_0	characteristic chamber dimension, 0.004 m
Z_∞	dimensionless outer boundary location.

Greek symbols

β	coefficient of volume expansion [K^{-1}]
ε	convergence criteria
ζ	dimensionless vorticity component in the ϕ-direction
θ	angular coordinate
μ	surrounding gas viscosity [$kg m^{-1} s^{-1}$]
ν	surrounding gas kinematic viscosity [$m^2 s^{-1}$]
ρ	surrounding gas density [$kg m^{-3}$]
ϕ	coordinate representing the angle of rotation about the axis of symmetry of the flow
ψ	dimensionless stream function
ω	relaxation factor.

Subscripts

G	vorticity
i	mesh point index in the z-direction
j	mesh point index in the θ-direction
r	radial direction
s	surface
T	temperature
w	general function
z	modified radial direction
∞	ambient
θ	tangential direction
ψ	stream function.

Superscripts

L	Lth iteration
$L-1$	$(L-1)$th iteration.

the drag force induced on a sphere by a natural convective flow field are found in the literature.

The classic references to analytical treatments of natural convection around spheres at small Grashof numbers are Mahony [11], Fendell [12], Hossain and Gebhart [13], and Hieber and Gebhart [14]. Each attempted to solve the problem by a perturbation method, but a suitable outer solution could not be obtained so as to match with the inner expansion. This problem can, however, be solved by a series truncation method [15] or using finite difference methods to obtain solutions [1, 2, 16, 17]. The Boussinesq approximation is used in all of the above-referenced studies. Only Geoola and Cornish [1, 2] calculate a natural convective drag force; all previous studies concentrate on the heat transfer aspects of the problem.

In this study experiments were performed in the electrodynamic balance to measure the natural convective drag force on a heated particle for Grashof

numbers of 0.002–0.03. These experiments were compared to both steady-state and transient finite difference solutions of the continuity, energy, and Navier–Stokes equations.

DIMENSIONAL ANALYSIS

Dimensional analysis reveals that

$$F_{nat} = \frac{\mu^2}{\rho} C_{DT} \tag{3}$$

where F_{nat} is the natural convective drag force (N), μ the surrounding gas viscosity (kg m^{-1} s^{-1}), ρ the surrounding gas density (kg m^{-3}), and C_{DT} the dimensionless drag force coefficient.

The dimensionless drag force coefficient is some unknown function of the Grashof number, Gr, and the Prandtl number, Pr, which are defined as follows:

$$Gr = g\beta(T_s - T_\infty)R^3/\nu^2$$

$$Pr = C_p\mu/k$$

where g is the gravitational acceleration (m s^{-2}), β the coefficient of volume expansion (K^{-1}), T_s the particle surface temperature (K), T_∞ the ambient gas temperature (K), R the particle radius (m), ν the gas kinematic viscosity (m^2 s^{-1}), C_p the gas heat capacity at constant pressure per unit mass (m^2 s^{-2} K^{-1}), and k the gas thermal conductivity (kg m s^{-3} K^{-1}).

Note that we have used the convention of Geoola and Cornish to define Gr, where R is used as the characteristic length instead of particle diameter. All gas properties are evaluated at the gas film temperature, T_f, defined as $(T_s+T_\infty)/2$. The value of β used in the definition of Gr is $1/T_\infty$. The numerical results will be presented primarily as a function of the dimensionless drag force coefficient and Grashof number. It should be noted that evaluating the surrounding gas properties at the ambient gas temperature or the particle surface temperature has little effect on the comparison between numerical and experimental results for the two gases utilized in this work. With both N_2 and CO_2, when the evaluation temperature of the gas properties are increased from the ambient temperature to the particle surface temperature, the Grashof number decreases and the factor, μ^2/ρ, increases. Numerically, when the Grashof number decreases, the predicted C_{DT} also decreases. Experimentally, the increase in the factor, μ^2/ρ, will by equation (3), cause C_{DT} to decrease also. This behavior of the surrounding gas properties with temperature makes the choice of evaluation temperature less critical.

THEORETICAL MODEL

A numerical technique modeled after that of Geoola and Cornish [1, 2] is used to solve the conservation equations of mass, momentum, and energy in two dimensions for the gas phase near the particle. Methods were developed to obtain both a steady-state and a transient solution. The governing equations are expressed in spherical polar coordinates $(\tilde{r},\theta,\phi)$. Radial distance, temperature, velocities, and time are nondimensionalized in the following manner:

$$r = \tilde{r}/R \tag{4}$$

$$T = (\tilde{T}-T_\infty)/(T_s-T_\infty) \tag{5}$$

$$u_r = \tilde{u}_r\tilde{r}/\nu \tag{6}$$

$$u_\theta = \tilde{u}_\theta\tilde{r}/\nu \tag{7}$$

$$t = \tilde{t}\nu/\tilde{r}^2 \tag{8}$$

where the tilde over a variable represents the dimensional form of the variable. The assumptions used in this model are that: (1) the particle is spherical; (2) the particle has a uniform, constant surface temperature; (3) the particle is not rotating; (4) flow is axisymmetric (all the dependent variables are independent of ϕ); (5) the only body force is gravity; (6) the Boussinesq approximation applies; and (7) other fluid properties (such as viscosity, specific heat, and thermal conductivity) are constant. The Navier–Stokes and continuity equations were combined and expressed in stream function–vorticity form. The energy, vorticity transport, and stream function equations are then transformed from polar coordinates (r,θ) to rectangular coordinates (z,θ) by means of the transformation

$$r = e^z. \tag{9}$$

The dimensionless energy conservation equation becomes

$$e^{2z}\frac{\partial T}{\partial t} + \frac{1}{e^z\sin\theta}\left(\frac{\partial\psi}{\partial z}\frac{\partial T}{\partial\theta} - \frac{\partial\psi}{\partial\theta}\frac{\partial T}{\partial z}\right) = \frac{1}{Pr}\left(\frac{\partial^2 T}{\partial z^2} + \frac{\partial T}{\partial z} + \frac{\partial^2 T}{\partial\theta^2} + \cot\theta\frac{\partial T}{\partial\theta}\right) \tag{10}$$

where the velocity components are

$$u_z = -\frac{1}{e^{2z}\sin\theta}\frac{\partial\psi}{\partial\theta} \tag{11}$$

$$u_\theta = \frac{1}{e^{2z}\sin\theta}\frac{\partial\psi}{\partial z}. \tag{12}$$

The vorticity transport equation is given by

$$e^{2z}\frac{\partial G}{\partial t} + \frac{1}{e^z\sin\theta}\left[\frac{\partial\psi}{\partial z}\left(\frac{\partial G}{\partial\theta} - 2G\cot\theta\right) - \frac{\partial\psi}{\partial\theta}\left(\frac{\partial G}{\partial z} - 2G\right)\right] = e^{2z}E^2(G) + e^{2z}Gr\sin^2\theta\left(\frac{\partial T}{\partial z} + \cot\theta\frac{\partial T}{\partial\theta}\right) \tag{13}$$

where G is the modified dimensionless vorticity, defined as

$$G = \zeta e^z\sin\theta. \tag{14}$$

The 'E^2' operator is defined as

$$e^{2z}E^2 = \frac{\partial^2}{\partial z^2} - \frac{\partial}{\partial z} + \frac{\partial^2}{\partial \theta^2} - \cot\theta\frac{\partial}{\partial \theta}. \quad (15)$$

The stream function equation is written as

$$e^{2z}G = e^{2z}E^2(\psi). \quad (16)$$

The steady-state boundary conditions are as follows.

At the sphere surface ($z = 0$):

$$\psi = 0$$

$$G = \frac{\partial^2\psi}{\partial z^2}$$

$$T = 1.$$

Along the axis of symmetry ($\theta = 0$ or π):

$$\psi = 0$$

$$G = 0$$

$$\frac{\partial T}{\partial \theta} = 0.$$

At the outer boundary ($z = z_\infty$):

$$\psi = \text{smooth}$$

$$G = \text{smooth}$$

$$T = 0.$$

The dependent variable is made smooth at the outer boundary by approximating its value using a first-order polynomial in z and specific values at the two adjacent nodes. The time-dependent terms were included in the energy and the vorticity transport equations for the transient solution. The initial conditions ($t = 0$) for the transient case are as follows:

$$\psi = 0 \text{ for all } z \text{ and } \theta$$

$$G = 0 \text{ for all } z \text{ and } \theta$$

$$T = 1 \text{ at } z = 0$$

$$T = 0 \text{ for all other } z.$$

Upon solution of the steady-state stream function, vorticity, and temperature, other quantities are calculated as follows [1, 2].

Local Nusselt number at the sphere surface:

$$Nu_\theta = -2\left.\frac{\partial T}{\partial z}\right|_{z=0}. \quad (17)$$

Average or overall Nusselt number:

$$Nu = \tfrac{1}{2}\int_0^\pi Nu_\theta \sin\theta\, d\theta. \quad (18)$$

Dimensionless pressure at the front stagnation point:

$$K_0 = 4\int_0^{z_\infty}\frac{\partial\zeta}{\partial\theta}dz - 2\int_0^{z_\infty}\frac{1}{e^z}\frac{\partial}{\partial t}\left(\frac{\partial^2\psi}{\partial\theta^2}\right)dz + 2Gr\int_0^{z_\infty} Te^z\, dz. \quad (19)$$

Dimensionless pressure at the sphere surface (surface pressure):

$$K_\theta = K_0 + 2Gr(1-\cos\theta) + 2\int_0^\theta\left(\frac{\partial\zeta}{\partial z} + \zeta\right)d\theta. \quad (20)$$

Dimensionless pressure drag (form drag):

$$C_{DP} = \int_0^\pi K_\theta \sin 2\theta\, d\theta. \quad (21)$$

Dimensionless viscous drag (frictional drag):

$$C_{DF} = 4\int_0^\pi \zeta_s \sin^2\theta\, d\theta. \quad (22)$$

Dimensionless total drag:

$$C_{DT} = C_{DP} + C_{DF}. \quad (23)$$

The integrands in equations (19) and (20) are evaluated at $\theta = 0$ and $z = 0$, respectively.

NUMERICAL METHOD

Finite differencing was used to solve equations (10), (13), and (16). Central differences were used to approximate the first-order derivatives of temperature, vorticity, and the stream function, except in the convective terms of the energy and vorticity equations where an upwind differencing method was used for stability purposes. The upwind or upstream differencing method utilizes backward differencing when the velocity of the fluid is positive and forward differencing when the velocity of the fluid is negative. Therefore, the one-sided difference is always on the upwind side of the node point. In the steady-state case, the energy, vorticity, and stream function equations were solved simultaneously using an extrapolated Gauss–Seidel method [18]. The Gauss–Seidel method updates the coefficients point by point using the following relationship:

$$W_{i,j}^{(L)} = W_{i,j}^{(L-1)} + \omega_w(W_{i,j}^{(L)} - W_{i,j}^{(L-1)}) \quad (24)$$

where W represents either temperature, vorticity, or the stream function, ω_w is a relaxation parameter used to accelerate the rate of convergence, and L is the iteration number. The convergence criteria used was

$$\sum_{i=1}^{M}\sum_{j=1}^{N}|W_{i,j}^{(L)} - W_{i,j}^{(L-1)}| < \varepsilon_w \quad (25)$$

for all three dependent variables: T, G, and ψ. For all the steady-state computations, $\varepsilon_T = 0.00001$, $\varepsilon_G = 0.001$, $\varepsilon_\psi = 0.0001$, $\omega_T = 1.5$, $\omega_G = 1.2$, and $\omega_\psi = 1.3$. In the transient computations, the energy and vorticity transport equations were solved using Peaceman and Rachford's ADI method [19]. The stream function equation was solved at each time step using an extrapolated Gauss–Seidel method. In both

the steady and transient cases derivative boundary conditions along the axis of symmetry were approximated by third-order polynomials and the derivative boundary conditions at the particle surface were approximated by fifth-order polynomials. The boundary conditions at the outer boundary were approximated by first-order polynomials.

The typical number of mesh points used in the calculations was $M = 100$ and $N = 31$, where M is the number of nodes in the r-direction and N the number of nodes in the θ-direction. Typical values of m and n, mesh spacings in the z- and θ-directions, respectively, were 0.04 and 0.1047.

DISCUSSION OF NUMERICAL RESULTS

Both the steady-state and transient solutions were solved with the same boundary conditions as Geoola and Cornish [1, 2] except at the outer boundary. Instead of forcing the vorticity and the stream function to zero at the outer boundary, these dependent variables were approximated by linear polynomial extrapolations in the z-direction using the values of the vorticity and the stream function at the two preceding nodes. For example, for the case of vorticity

$$G(z_\infty, j) = 2G(z_\infty - 1, j) - G(z_\infty - 2, j). \quad (26)$$

When the vorticity and the stream function are forced to zero, no mass is allowed to leave through the outer boundary. Therefore, a recirculation pattern is set up. When the vorticity and stream function at the outer boundary are not set to zero and are approximated using adjacent values, mass is permitted to cross the outer boundary, and no recirculation pattern is set up. Gas flows into the bottom of the outer sphere and out of the top. The overall drag coefficient was found to be independent of the type of outer boundary condition used as long as the outer boundary tended toward infinity. The drag coefficient was found to be very sensitive to grid size in the radial direction until some critical grid size was obtained, however. Figure 1 is a plot of the computed steady-state drag coefficient (C_{DT}) for $Gr = 0.05$ vs location of the outer boundary for the two types of outer boundary conditions examined. The value of the critical grid size was a function of the outer boundary condition used. If the outer boundary condition approximates the vorticity and stream function using adjacent values, the critical grid size is 50 times the radius of the particle. If Geoola and Cornish's boundary conditions are used, the critical grid size is at least 120 times the radius of the particle. The former type of outer boundary condition is preferred because it is physically more realistic and because of the savings in computer storage and computational time. Therefore, the boundary condition allowing mass flow through the outer boundary is utilized for all of the cases examined in this paper. The grid size used by Geoola and Cornish [1, 2] was below the critical grid size; they had an outer boundary at 24.5 radii away from the particle surface and

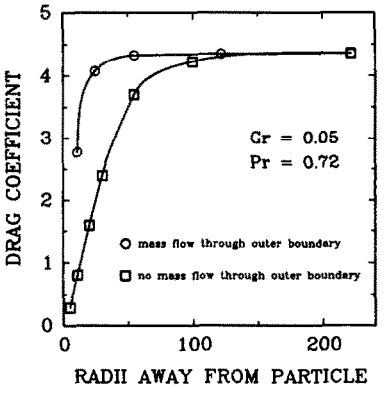

FIG. 1. Computed steady-state drag force coefficient for $Gr = 0.05$ and $Pr = 0.72$ vs location of the outer boundary with type of outer boundary condition as a parameter.

reported a drag coefficient of 1.17. If the outer boundary is placed farther away from the particle, past the critical grid size of 120 times the radius of the particle, a dimensionless drag force coefficient of 4.33 would have been calculated.

Figure 2 is a plot of the steady-state dimensionless pressure, viscous, and total drag coefficients, as well as Nusselt number vs Grashof number. The ratio of the dimensionless viscous drag over the dimensionless pressure drag remains constant at a value of 2.0 over the range of Grashof numbers examined. This implies that there is no change in the basic flow patterns, such as the separation of the boundary layer. The Nusselt number asymptotically approaches 2.0 as Grashof number goes to zero.

The steady-state drag force coefficient was found to have a weak negative dependence on Prandtl number. For the gases and temperature range examined experimentally, the Prandtl number would have a maximum of 0.78 and a minimum of 0.69. This corresponds to only a 3.5% difference in the dimensionless drag force coefficient. Therefore, for the purposes of this paper, the dimensionless drag force coefficient will be assumed to only be a function of the Grashof number.

Figure 3 is a plot of the total drag force coefficient

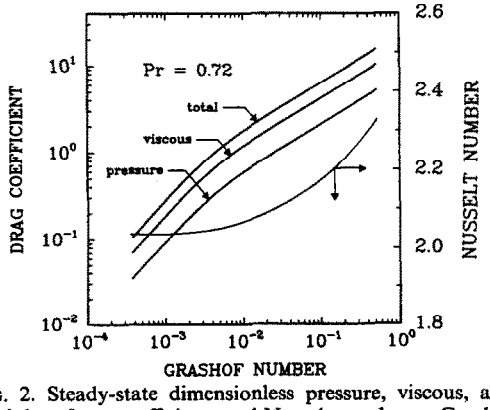

FIG. 2. Steady-state dimensionless pressure, viscous, and total drag force coefficients and Nusselt number vs Grashof number for $Pr = 0.72$.

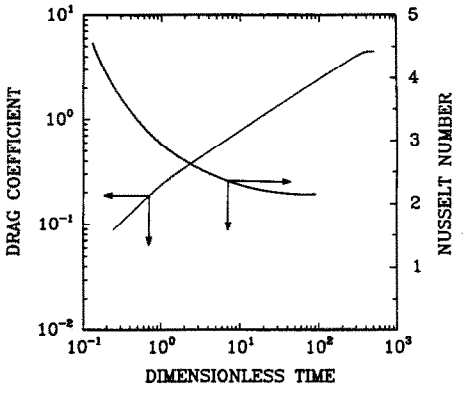

FIG. 3. Total drag force coefficient and Nusselt number vs dimensionless time for $Gr = 0.05$ and $Pr = 0.72$.

and Nusselt number vs dimensionless time for $Gr = 0.05$ and $Pr = 0.72$. The transient drag coefficient is within 10% of steady state at a dimensionless time of 280. The Nusselt number is within 10% of steady state at a dimensionless time of 15. The Nusselt number reaches steady state in less than 1/10 of the time it takes the drag force coefficient to reach steady state. This indicates that the temperature profile is set up one order of magnitude faster than the flow field.

Figure 4 is a log–log plot of the dimensionless time required to reach 90% of the steady-state total drag force coefficient vs Grashof number. As Grashof number increases, the dimensionless time decreases.

Figure 5 is a plot of the steady-state dimensionless tangential velocity at $\theta = 90°$ vs radial distance from the particle for Grashof numbers of 0.5, 0.05, and 0.005. Superimposed on this plot is the dimensionless temperature profile, which is essentially the same for these three Grashof numbers. The outer boundary used in this case was 52 radii away from the sphere center but the variables of interest are only shown out to 20 radii away from the sphere to give more spatial resolution near the sphere's surface. The maximum dimensionless velocity increases with increasing Gr. Also, the radial distance at which the maximum

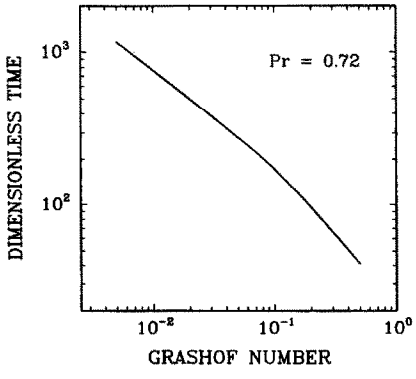

FIG. 4. Dimensionless time required to reach 90% of the steady-state total drag force coefficient vs Grashof number for $Pr = 0.72$.

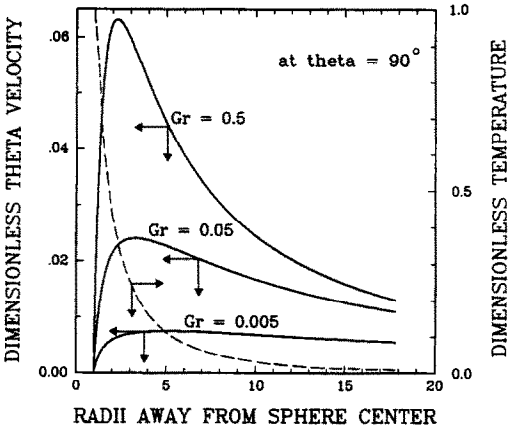

FIG. 5. Steady-state tangential velocity at $\theta = 90°$ and dimensionless temperature vs radial distance from the particle for $Gr = 0.005$, 0.05, and 0.5.

dimensionless velocity occurs moves closer to the particle surface with increasing Gr.

A more complete description of the numerical method and the results are presented by Dudek and Fletcher [20].

EXPERIMENTAL APPARATUS

Experiments were performed in an electrodynamic balance to measure the natural convective drag force on spherical, inert particles. The theory of the balance is described by Wuerker *et al.* [21], Davis and Ray [22], and Spjut [4]. The electrodynamic balance, shown schematically in Fig. 6, is capable of suspending a single, charged, 1–250 μm diameter particle in a dynamic electric field. The balance itself consists of three electrodes separated by Teflon insulation. The a.c. ring electrode, which is attached to an a.c. voltage with a peak-to-peak voltage of 5000 V at 100 Hz, gives the particle lateral stability. The top and bottom endcap electrodes provide a vertical d.c. field that can be adjusted to counteract the gravitational force on the particle. If the top electrode is connected to a positive d.c. voltage and the bottom electrode is connected to a negative d.c. voltage, then a negatively charged particle can be suspended. The particle may be raised or lowered in the balance by varying the d.c. voltage across the top and bottom electrodes. When the particle is balanced in the center of the chamber, the d.c. voltage across the electrodes is proportional to the particle mass divided by the excess particle charge. Optical access to the suspended particle is through the four holes in the ring electrode, the holes in the top and bottom electrodes, or the holes along the asymptotes between the electrodes.

The suspended particle is illuminated by either a 5 mW He–Ne laser or a quartz halogen lamp, and can be observed with an optical microscope (70×). The particle diameter can be measured to within ± 3 μm using a graticule located in the eyepiece of the microscope. Some of the scattered He–Ne light from the

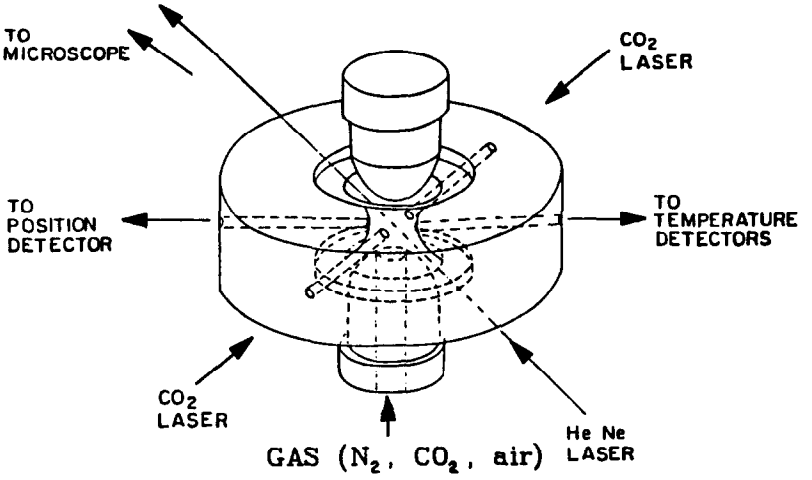

FIG. 6. Exploded view of the electrodynamic balance.

particle can also be collected and sent to an electro-optical position control system which automatically adjusts the d.c. voltage required for particle balancing.

The suspended particle is heated from two sides by a 20 W carbon dioxide laser with a nominal wavelength of 10.6 μm, and particle temperature is measured via two color (2 and 4 μm) infrared pyrometry. The particle's environment may be altered by introducing various gases into the chamber through the bottom electrode. The experimental apparatus used in these experiments is described fully by Spjut [4].

MASS MEASUREMENT BY THE AERODYNAMIC DRAG FORCE TECHNIQUE

Various techniques have been used for sizing of particles suspended in an electrodynamic balance [22–24] and electron stepping [25, 26] has been used for absolute mass and charge measurement. The electron stepping method involves measuring the change in balancing voltage associated with the removal of a single electron from the particle surface. Unfortunately, this method can only be used on particles less than 20 μm in diameter due to the large number of excess charges (>1 million) required to balance a larger particle. Larger spherical particles may be weighed by an aerodynamic drag force technique [23]. This technique involves measuring the aerodynamic drag force on the particle as a function of the flow rate of gas through the chamber and using Stokes' law to back out the particle mass. By performing a vertical force balance on the particle

$$mg = qE + F_{\text{Stokes}} \tag{27}$$

where m is the particle mass (kg), g the gravitational acceleration = 9.81 m s^{-2}, q the total excess charge (C), E the electric field strength in the vertical direction (V cm^{-1}), and F_{Stokes} the Stokes' drag force (N), or since

$$E = V_{\text{d.c.}} C / z_0 \tag{28}$$

and

$$F_{\text{Stokes}} = 6\pi R \mu v \tag{29}$$

where $V_{\text{d.c.}}$ is the balancing d.c. voltage across endcap electrodes (V), C the chamber constant = 0.4 (dimensionless), z_0 the characteristic chamber dimension = 0.004 m, R the particle radius (m), μ the surrounding gas viscosity (kg s^{-1} m^{-1}), and v the velocity of the surrounding gas (m s^{-1}).

Since the only unknowns are m and q, if $V_{\text{d.c.}}$ is measured for two gas velocities, both m and q may be determined. A typical weighing involves measuring the balancing d.c. voltage at seven different gas velocities. The aerodynamic drag force technique of weighing requires approximately 10 min when performed as described above, and has successfully measured particle masses as small as 1.0×10^{-6} g.

EXPERIMENTAL PARAMETERS AND PROCEDURES

A synthetic char with a trade name 'Spherocarb' manufactured by Foxboro/Analabs was used for all the drag force measurements. 'Spherocarb' particles were used for several reasons. First, they are very spherical. This enables them to be weighed by the aerodynamic drag force method. 'Spherocarb' sphericity also promotes more uniform particle heating which helps minimize thermophoretic forces (forces induced on the particle due to temperature gradients on the surface). Secondly, the 'Spherocarb' particles are approximately black at the wavelengths of interest. Thirdly, the available size range of 'Spherocarb' particles (125–250 μm) allows particle diameter measurements to be made optically using a microscope. Also, the large size increases the magnitude of the 2.0 and 4.0 μm signals reaching the pyrometers, allowing for more accurate temperature measure-

ment. Finally, the large size helps to reduce the relative magnitude of the thermophoretic forces exerted on the particle.

Experiments were performed varying three parameters: particle diameter, particle temperature, and surrounding gas. Particle diameter was varied between 127 and 236 μm. Particle temperature ranged from 600 to 1200 K. Two surrounding gases were used, nitrogen and carbon dioxide.

An experiment is initiated by injecting 'Spherocarb' particles into the electrodynamic balance using a syringe. After adjusting the a.c. and d.c. fields to eliminate all but a single 'Spherocarb' particle, nitrogen is purged through the chamber at 20 ml min^{-1} for 20 min. The diameter of the particle is measured to ± 3 μm with the microscope and a graticule. The particle is then weighed two times using the aerodynamic drag force technique. If the two weights deviate by more than 5%, a third weighing is performed or the particle is discarded and a new particle captured. Once the particle has been weighed, the nitrogen atmosphere in the chamber is maintained using a steady flow of 5 ml min^{-1} of nitrogen. The carbon dioxide laser is then turned on and warmed up for approximately 20 min in order to reduce fluctuations in the power to approximately $\pm 15\%$. After the carbon dioxide laser is warmed up, the balancing voltage is recorded to within ± 0.1 V and the laser heating of the particle initiated. The d.c. balancing voltage is adjusted to balance the natural convective drag force and recorded to within ± 0.5 V along with the 2 and 4 μm detector signals used for particle temperature measurement. Particle temperatures could be measured to within ± 20 K.

Typical changes in balancing voltage and particle temperature for a 'Spherocarb' particle undergoing a heating/cooling cycle are shown in Fig. 7. At time zero, the particle is balanced in the chamber and is at ambient temperature. Laser heating begins at 0.28 s and ends at 1.94 s. After the particle is heated to above 600 K, the natural convective drag force develops and the voltage required for balancing decreases.

A force balance on the heated particle reveals that

$$\Delta V/V_i = F_{\text{nat}}/mg \qquad (30)$$

where ΔV is the change in balancing voltage between an unheated and a heated particle (V), V_i the balancing voltage of an unheated particle (V), F_{nat} the natural convective drag force (N), and mg the particle weight (N).

When heating is discontinued, the balancing voltage should equal the initial balancing voltage. This serves as a check that the particle charge to mass ratio did not change during the experiment. This process is repeated 5–15 times with varying carbon dioxide laser powers; i.e. varying particle temperatures. The particle is also periodically reweighed to provide a check that the particle mass did not change. Carbon dioxide is then purged through the chamber and the process is repeated.

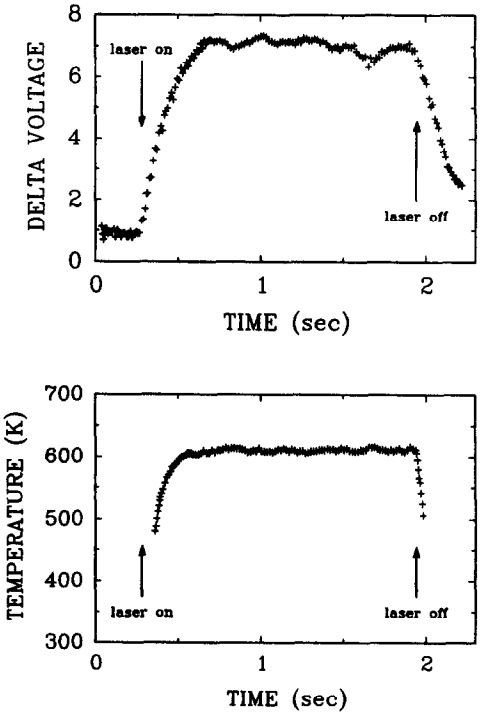

FIG. 7. Change in balancing voltage and temperature vs time for a 'Spherocarb' particle heated to 610 K.

COMPARISON OF EXPERIMENTAL AND NUMERICAL RESULTS

Five different 'Spherocarb' particles with diameters of 127, 153, 168, 192, and 236 μm were examined experimentally. The steady-state drag force coefficient vs Grashof number is plotted in Fig. 8. The triangles represent experiments performed in nitrogen, the circles represent experiments performed in carbon dioxide, and the solid line represents the numerical solution. The surrounding gas properties are evaluated at the film temperature which is defined as the arithmetic mean between the particle surface temperature and the ambient gas temperature. The numerical solution agrees well with the experimental results, even though the Boussinesq criterion has been

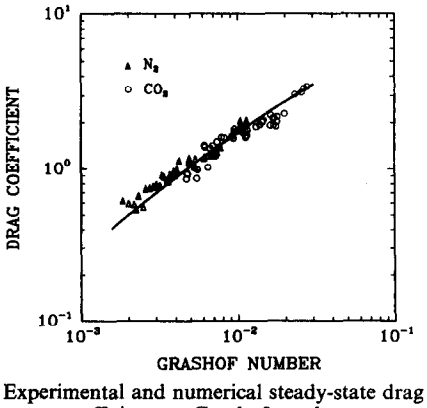

FIG. 8. Experimental and numerical steady-state drag force coefficients vs Grashof number.

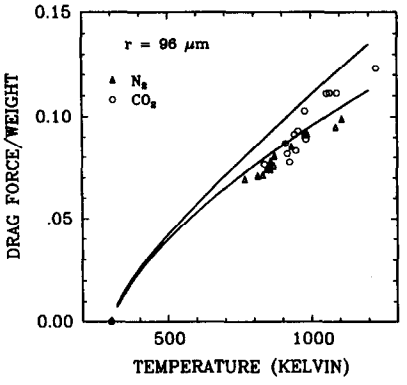

FIG. 9. Experimental measurements and numerical calculations of the natural convective drag force/particle weight vs particle temperature for a 'Spherocarb' particle with a radius of 96 μm.

violated due to the large temperature differences in the problem [27].

Figure 9 is a plot of steady-state natural convective drag force divided by particle weight vs particle temperature. This particular run was performed in two different surrounding gases (nitrogen and carbon dioxide) on a 'Spherocarb' particle with a radius of 96 μm. Again, the triangles represent experiments performed in nitrogen, the circles represent experiments performed in carbon dioxide, the top solid line represents the carbon dioxide numerical solution, and the bottom solid line represents the nitrogen numerical solution. At room temperature, the drag force is equal to zero.

Figure 10 is a plot of the change in balancing voltage vs real time for a 183 μm diameter 'Spherocarb' particle heated to 610 K in nitrogen. The initial, unheated voltage was 100 V. The small points represent experimental results and the smooth solid line represents the transient numerical solution. The experimental points were smoothed with a moving average filter. Again we see good agreement between experiment and theory. According to the heat transfer model developed by Spjut [4], the particle should reach 90% of its equilibrium temperature in 70–80 ms.

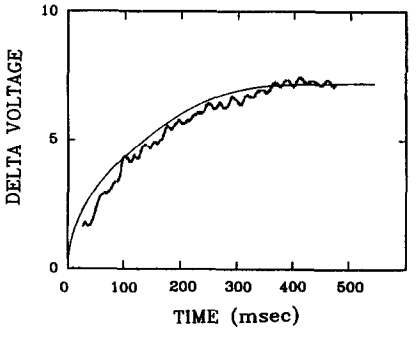

FIG. 10. Experimental and numerical changes in balancing voltage vs time for a 183 μm diameter 'Spherocarb' particle heated to 610 K in nitrogen.

PRACTICAL IMPLICATIONS

Since the steady-state program takes approximately 5–15 min on a VAX 8600, it is desirable to approximate the numerical solution, shown graphically in Fig. 2, by a correlation. A discrete least squares method [28] was used to obtain the following second-order polynomial which describes the steady-state dimensionless total drag force coefficient:

$$\log(C_{DT}) = 1.25 + 0.31[\log(Gr)] - 0.097[\log(Gr)]^2. \quad (31)$$

This correlation is good to within 5% over the range $0.004 < Gr < 0.5$ for $Pr = 0.72$.

The transient program takes approximately 5–24 h on a VAX 8600. The same discrete least squares method was used to obtain the following second-order polynomial that approximates the dimensionless time required to reach 90% of the steady-state drag force coefficient

$$\log(t_{90}\%) = 1.32 - \log(Gr) - 0.11[\log(Gr)]^2. \quad (32)$$

Figure 11 is a plot of the numerical solution of the steady-state natural convective drag force for a heated sphere in ambient nitrogen divided by the particle weight vs particle radius for a particle density of 500 kg m^{-3} and three different particle surface temperatures, 1500, 900, and 500 K. The circles represent predictions of the drag force/weight using the numerical solution and the solid lines are 'best fit' lines through these points. The numerical solution predicts a peak in drag force divided by weight for a particle radius of approximately 40 μm. The numerical solution predicts that the natural convective drag force around aerosol particles less than 10 μm in diameter with a density greater than 500 kg m^{-3} will be less than 5% of the particle weight if particle temperatures are kept under 1500 K. Furthermore, since the drag force divided by weight is inversely proportional to particle density, heavy particles with densities greater than 2500 kg m^{-3} will also not experience drag forces greater than 5% of their weights if particle temperatures are kept under 1500 K.

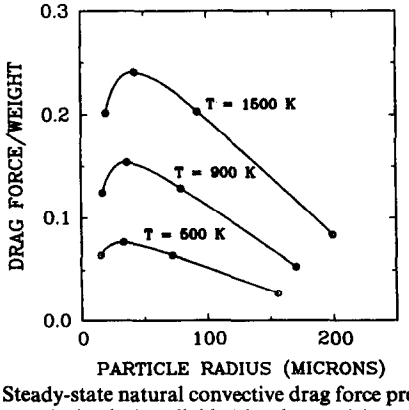

FIG. 11. Steady-state natural convective drag force predicted by the numerical solution divided by the particle weight vs particle radius for a particle density of 500 kg m^{-3} and three different particle surface temperatures, 1500, 900, and 500 K.

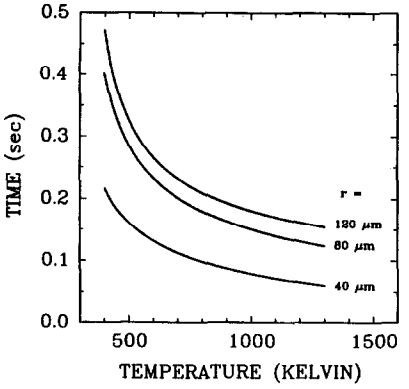

FIG. 12. Numerical predictions of real time required to reach 90% of the steady-state drag force coefficient vs particle temperature for three different particle radii of 40, 80, and 120 μm.

Figure 12 is a prediction based on the transient numerical results of the real time required to reach 90% of the steady-state drag coefficient in nitrogen vs particle temperature for three different particle radii of 40, 80, and 120 μm. The time required to set up the natural convective flow field decreases with increasing particle temperature and decreases with decreasing particle radius.

For slow reactions, when the time required to set up the natural convective flow field is much less than the time required for chemical reaction, the steady-state solution can be used to describe the natural convective drag throughout the reaction. This allows the use of the electrodynamic balance to follow mass in a continuous fashion. For fast reactions, when the time required to set up the natural convective flow field is slightly less than the time required for chemical reaction, the transient solution can be used to predict the natural convective drag throughout the reaction. For very fast reactions, when the time required to set up the natural convective flow field is longer than the time required for chemical reaction, the transient solution cannot be used to predict the natural convective drag, therefore, discrete mass vs time points will still be necessary.

CONCLUSIONS

The computational method of Geoola and Cornish [1, 2] for describing the heat transfer and fluid mechanics surrounding a heated solid sphere was modified to correctly calculate the drag force due to natural convection. The computer calculations were used to develop a correlation to approximate this drag force. An expression was also developed to approximate the time required to reach 90% of the steady-state drag coefficient.

The experimental steady-state and transient results of the natural convective drag force agree well with the Boussinesq numerical solutions, indicating that the Boussinesq approximation is valid over the experimental parameter range examined.

The numerical solution predicts that the steady-state natural convective drag force relative to the particle weight should increase with particle radius up to a maximum value at a particle radius of approximately 40 μm and then start to decrease. Therefore, the natural convective drag force around aerosol particles, heated to under 1500 K, with radii less than 5 μm and density greater than 500 kg m^{-3} should be less than 5% of the particle weight.

The steady-state natural convective drag force relative to particle weight is inversely proportional to particle density. Therefore, if a particle is to be heated to a temperature under 1500 K and has a density greater than 2500 kg m^{-3}, its natural convective drag force should be less than 5% of the particle weight.

The time required to set up the natural convective flow field decreases with increasing particle temperature and decreases with decreasing particle radius. The time was in the range of 100–300 ms for the experiments performed. This relatively 'slow' natural convective drag force may prevent continuous mass vs time measurements in the electrodynamic balance for certain fast reactions.

Acknowledgement—This work was funded by Exxon Research and Engineering Corporation.

REFERENCES

1. F. Geoola and A. R. H. Cornish, Numerical solution of steady-state free convective heat transfer from a solid sphere, *Int. J. Heat Mass Transfer* **24**, 1369–1379 (1981).
2. F. Geoola and A. R. H. Cornish, Numerical simulation of free convective heat transfer from a sphere, *Int. J. Heat Mass Transfer* **25**, 1677–1687 (1982).
3. S. Arnold and M. Lewittes, Size dependence of the photophoretic force, *J. Appl. Phys.* **53**(7), 5314–5319 (1982).
4. R. E. Spjut, Ph.D. Thesis, Massachusetts Institute of Technology, Cambridge, Massachusetts (1985).
5. P. Meyer, Heat transfer to small particles by natural convection, *Inst. Chem. Engrs* **15**, 127–131 (1937).
6. W. Elenbaas, The dissipation of heat by free convection of spheres and horizontal cylinders, *Physica* **9**(3), 285–296 (1942).
7. W. E. Ranz and W. R. Marshall, Jr., Evaporation from drops, *Chem. Engng Prog.* **48**(4), 173–180 (1952).
8. W. G. Mathers, A. J. Madden, Jr. and E. L. Piret, Simultaneous heat and mass transfer in free convection, *Ind. Engng Chem.* **49**(6), 961–968 (1957).
9. T. Tsubouchi and S. Sato, Heat transfer from fine wires and particles by natural convection, *Res. Inst. High Speed Mech., Tohoku Univ.* **12**, 127–132 (1960).
10. T. Yuge, Experiments on heat transfer from spheres including combined natural and forced convection, *Trans. ASME* **C82**, 214–220 (1960).
11. J. J. Mahony, Heat transfer at small Grashof numbers, *Proc. R. Soc. London* **A238**, 412–423 (1956).
12. F. E. Fendell, Laminar natural convection about an isothermally heated sphere at small Grashof number, *J. Fluid Mech.* **34**(1), 163–176 (1968).
13. M. A. Hossain and B. Gebhart, Natural convection about a sphere at low Grashof number. *Fourth International Heat Transfer Conference*, Versailles, Paris, Vol. 5, NCl. 6. A.I.Ch.E., New York (1970).
14. C. A. Hieber and B. Gebhart, Mixed convection from a sphere at small Reynolds and Grashof numbers, *J. Fluid Mech.* **38**(1), 137–159 (1969).

15. S. N. Singh and M. M. Hasan, Free convection about a sphere at small Grashof number, *Int. J. Heat Mass Transfer* **26**, 781–783 (1983).
16. B. Farouk, Natural convection heat transfer from an isothermal sphere, *Therm. Sci.* **16**(1), 347–364 (1982).
17. T. Fujii, T. Honda and M. Fujii, A numerical analysis of laminar free convection around an isothermal sphere: finite-difference solution of the full Navier–Stokes and energy equations between concentric spheres, *Numer. Heat Transfer* **7**, 103–111 (1984).
18. G. D. Smith, *Numerical Solution of Partial Differential Equations*, Chaps 2 and 5. Oxford University Press, London (1965).
19. D. W. Peaceman and H. H. Rachford, Jr., The numerical solution of parabolic and elliptic differential equations, *J. Soc. Ind. Appl. Math.* **3**, 28–41 (1955).
20. D. R. Dudek and T. H. Fletcher, Numerical calculation of the drag force induced by natural convection on spheres at low Grashof numbers, Sandia National Laboratory Report, SAND87-8201 (Feb. 1987).
21. R. F. Wuerker, H. Shelton and R. V. Langmuir, Electrodynamic containment of charged particles, *J. Appl. Phys.* **30**(3), 342–349 (1959).
22. E. J. Davis and A. K. Ray, Single aerosol particle size and mass measurements using an electrodynamic balance, *J. Colloid Interface Sci.* **75**(2), 566–576 (1980).
23. E. J. Davis and R. Periasamy, Light-scattering and aerodynamic size measurements for homogeneous and inhomogeneous microspheres, *Langmuir* **1**, 373–379 (1985).
24. G. Sageev, J. H. Seinfeld and R. C. Flagan, Particle sizing in the electrodynamic balance, *Rev. Scient. Instrum.* **57**(5), 933–936 (1986).
25. S. Arnold, Determination of particle mass and charge by one electron differentials, *J. Aerosol Sci.* **10**, 49–53 (1979).
26. M. A. Philip, F. Gelbard and S. Arnold, An absolute method for aerosol particle mass and charge measurement, *J. Colloid Interface Sci.* **91**(2), 507–515 (1983).
27. J. Boussinesq, *Theorie analytique de la chaleur*, Vol. 2. Gathier-Villars, Paris (1903).
28. R. L. Burden, J. P. Faires and A. C. Reynolds, *Numerical Analysis*, pp. 136–145. Prindle Weber & Schmidt, Boston, Massachusetts (1978).

FORCES DE TRAINEE INDUITES PAR CONVECTION NATURELLE SUR DES SPHERES AUX FAIBLES NOMBRES DE GRASHOF: COMPARAISON DE LA THEORIE ET DE L'EXPERIENCE

Résumé—Quand une sphère solide chaude est introduite dans un fluide ambiant, se produit un écoulement de convection naturelle et il en résulte une force de trainée sur la sphère. Pour des particules de diamètre 10–250 μm, la force de trainée peut être aussi grande que le poids de la particule. Cette étude couvre les mesures expérimentales et le calcul numérique pour les régimes permanent et variable de convection naturelle aux faibles nombres de Grashof. Les mesures de trainée sont faites à l'aide d'une balance électrodynamique pour des nombres de Grashof allant de 0,002 à 0,03. Les solutions numériques, basées sur des techniques de Geoola et Cornish (*Int. J. Heat Mass Transfer* **24**, 1369–1379 (1981); **25**, 1677–1687 (1982)), sont obtenues pour des nombres de Grashof allant de 0,0004 à 0,5. La comparaison des résultats numériques et expérimentaux est satisfaisante.

WIRKUNG EINER AUFTRIEBSSTRÖMUNG AUF KUGELN BEI KLEINER GRASHOF-ZAHL: VERGLEICH VON THEORIE UND EXPERIMENT

Zusammenfassung—Wenn ein kugelförmiger erwärmter Festkörper in eine Flüssigkeit getaucht wird, wirkt durch die sich einstellende natürliche Konvektionsströmung eine Schleppkraft auf ihn. Für Teilchendurchmesser von 10–250 μm ist die Schleppkraft von gleicher Größenordnung wie das Gewicht des Teilchens. Die Untersuchung umfaßt die Messung und die numerische Berechnung der Schleppkraft durch natürliche Konvektion (stationär und transient) um Kugeln bei kleiner Grashof-Zahl. Die Messungen werden in einem elektrodynamischen Gleichgewicht für Grashof-Zahlen von 0,002 bis 0,03 durchgeführt. Numerische Lösungen unter Benutzung der Techniken von Geoola und Cornish (*Int. J. Heat Mass Transfer* **24**, 1369–1379 (1981); **25**, 1677–1687 (1982)) werden für Grashof-Zahlen von 0,0004 bis 0,5 angewandt. Experimentelle und numerische Ergebnisse zeigen eine gute Übereinstimmung.

СИЛЫ СОПРОТИВЛЕНИЯ, ВЫЗВАННЫЕ ЕСТЕСТВЕННОЙ КОНВЕКЦИЕЙ НА СФЕРАХ ПРИ МАЛЫХ ЧИСЛАХ ГРАСГОФА: СРАВНЕНИЕ ТЕОРИИ И ЭКСПЕРИМЕНТА

Аннотация—При размещении нагретой твердой сферы в жидкости возникает естественноконвективное течение, воздействующее на сферу. Для частиц диаметром 10–250 мкм сила сопротивления может быть равна весу частицы. Работа включает экспериментальное измерение и численный расчет силы сопротивления в условиях стационарного и переходного рехимов естественной конвекции вокруг сфер при малых числах Грасгофа. Экспериментальные измерения проводились при условиях электродинамического баланса для чисел Грасгофа в диапазоне от 0,002 до 0,03. Численные решения, полученные с помощью методики, используемой Джеолой и Корнишем (*Int. J. Heat Mass Transfer* **24**, 1369–1379 (1981); **25**, 1677–1687 (1982)), проведены для чисел Граспофа от 0,0004 до 0,5. Получено хорошее соответствие результатов экспериментов и численных расчетов.